Microscopic model for fracture of crystalline Si nanopillars during lithiation

CrossMark

Ill Ryu [a,*], Seok Woo Lee [b], Huajian Gao [a], Yi Cui [b], William D. Nix [b]

[a] School of Engineering, Brown University, Providence, RI 02912, USA
[b] Department of Materials Science and Engineering, Stanford University, Stanford, CA 94305, USA

HIGHLIGHTS

- We model lithiation in crystalline Si anode based on discrete phase boundary motion.
- Anisotropic phase boundary motion is taken into account.
- Microscopic model is derived to explain size-dependent fracture during lithiation.
- We estimate the work of fracture of lithiated Si.

ARTICLE INFO

ABSTRACT

Silicon (Si) nanostructures are attractive candidates for electrodes for Li-ion batteries because they provide both large specific charging capacity and less constraint on the volume changes that occur during Li charging. Recent experiments show that crystalline Si anodes expand highly anisotropically through the motion of a sharp phase boundary between the crystalline Si core and the lithiated amorphous Si shell. Here, we present a microscopic model to describe the size-dependent fracture of crystalline Si nanopillars (NPs) during lithiation. We derive a traction–separation law based on the plastic growth of voids, which, in turn, is used in a cohesive zone-finite element model. The model allows for both the initiation of cracking and crack growth. The initial size and spacing of the nanovoids, assumed to be responsible for the fracture, together with the computed facture toughness, are chosen to conform to recent experiments which showed the critical diameter of Si NPs to be 300–400 nm. The anisotropy of the expansion is taken into account and that leads naturally to the observed anisotropy of fracture. The computed work of fracture shows good agreement with recent experimental results and it may be possible to use it to describe the failure for other loading and geometries.

1. Introduction

High-capacity lithium-ion batteries (LIBs) have attracted much attention as a key element for portable electronic devices and electric vehicles [1,2]. The search for anode materials with high charging capacity has identified silicon (Si) as one of the most promising candidates, because it has an exceptionally high specific charging capacity of 4200 mAh g^{-1} [3]. However, the associated huge volume expansion during lithiation, can cause pulverization and capacity loss [4,5], thus impeding the development of Si anodes. To avoid the mechanical degradation due to lithiation-induced stresses, various nanostructures have been suggested as possible electrodes for improved cycling performance and fracture

resistance. Examples include nanowires [6], thin films [7,8], core–shell structures [9], and hollow structures [10,11].

Recent experiments have shown that lithiation of crystalline Si differs from that for amorphous Si: the lithiation process for crystalline Si involves a two-phase reaction, with an atomistically sharp phase boundary existing between the amorphous Li$_x$Si shell and the pristine crystalline Si core [12,13]. Moreover, the phase boundary moves faster in the <110> direction of crystalline Si than other directions [12,14,15]. These phenomena differ from the lithiation of amorphous Si, where lithiation is governed mainly by diffusion.

In an effort to understand the lithiation process for crystalline Si, and especially to understand the stress evolution and fracture, several authors have analyzed the stress evolution and deformation associated with interface reaction-controlled lithiation. Zhao et al. [16] developed an analytical model for concurrent interface

* Corresponding author. Tel.: +1 6507140731; fax: +1 4018639025.
E-mail addresses: ill_ryu@brown.edu, ryuill1@gmail.com (I. Ryu).

reaction and plasticity in nano-spheres. Pharr et al. [17] developed a kinetics-based model for anisotropic motion of phase boundaries by specifying phase boundary motion and computing morphology changes associated with lithiation, similar to those found experimentally [18]. By adjusting the diffusivity of lithium ions to simulate a sharp boundary, Yang et al. [19] also developed a model to show the anisotropic shape changes. In addition, McDowell et al. [20] have suggested a kinetics model to account for the effect of stress on the interface reaction rate.

In the present study, we have developed a microscopic model to explore size-dependent fracture of crystalline Si nanopillars (NPs) during lithiation. As a first approximation, we model the phase boundary motion by specifying a temperature field, using the analogy between thermal expansion and lithiation-induced swelling. Using this model, we can simulate the anisotropic expansion and accompanying stress evolution during the lithiation of crystalline Si NPs with various crystallographic orientations.
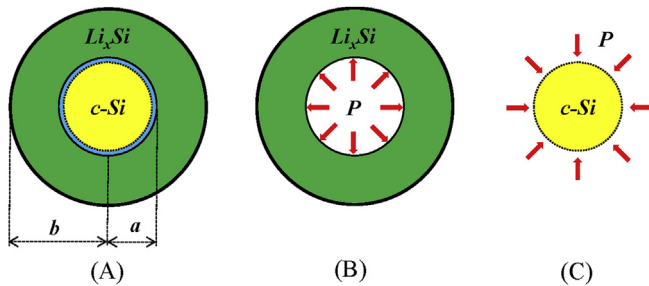
To model the crack initiation and propagation, we first derive a traction–separation law based on a microscopic description of the plastic growth of voids. From the traction–separation law, the work of fracture (G_c) is estimated by taking the initial size and spacing of the nanovoids such that a critical diameter of Si NPs of 300–400 nm is predicted, consistent with experiment.

We also performed experiments to determine the critical diameter for fracture of Si NPs during lithiation for different crystallographic orientations. We used the scanning electron microscope (SEM) to observe the shapes of individual pillars after lithiation, as done previously [18]. These experiments are then directly compared with the modeling results and the comparison leads to a good agreement on the size effect on fracture. This characterization method determines a critical diameter for fracture and also serves as a standard to judge the validity of our modeling.

2. Stress evolution during lithiation

2.1. Isotropic expansion model

Recent transmission electron microscopy (TEM) studies showed that a sharp phase boundary exists between crystalline Si and amorphous Li_xSi, thus creating a core–shell structure during lithiation of a crystalline Si NP [13,21,22]. As a first approximation, we start with the isotropic expansion model. To derive an approximate analytical solution for the stresses during lithiation, we divide the domain between the crystalline Si core and the amorphous Li_xSi shell, as shown in Fig. 1A. In this model, crystalline Si and the amorphous Li_xSi are assumed to be elastic and elastic–plastic, respectively. When the phase boundary moves during lithiation, we

Fig. 1. Schematic of lithiation of a crystalline Si nanopillar (A) At a given time, pristine silicon core and Li_xSi alloy shell. The thin layer (blue color) stands for the atomically sharp phase boundary only where lithiation occur at the given time duration. (B) Stress state of the lithiated Si alloy shell. (C) Stress state of pristine Si core. (For interpretation of the references to color in this figure legend, the reader is referred to the web version of this article.)

the interface reaction involving the breaking of Si–Si bonds and the forming of Li–Si bonds is assumed to occur only in an atomically thin layer (blue color in Fig. 1A). Due to the volume expansion of the thin layer between the core and shell, the surrounding Li_xSi shell can be considered to be in the same stress state as a pressurized cylindrical tube, with the core being subjected to a uniform radial pressure, as shown in Fig. 1B and C. [16,19,23]. Following Hill's treatment of a pressurized tube with the Tresca yield criterion [24], the stresses in the Li_xSi shell would then be

$$\left(\frac{\sigma_{rr}}{Y}\right)_{Li_xSi} = -\ln\left(\frac{b}{r}\right), \quad \left(\frac{\sigma_{\theta\theta}}{Y}\right)_{Li_xSi} = 1 - \ln\left(\frac{b}{r}\right), \quad (1a,b)$$

after assuming that the tube deforms fully plastically due to the large volume expansion. σ_{rr}, $\sigma_{\theta\theta}$ and Y are radial, tangential and yield stress, respectively. b is the outer radius of tube and r is the distance from the center. The corresponding stresses in the Si core would be

$$\left(\frac{\sigma_{rr}}{Y}\right)_{Si} = \left(\frac{\sigma_{\theta\theta}}{Y}\right)_{Si} = -\ln\left(\frac{b}{a}\right), \quad (2a,b)$$

where a is the radius of the Si core. From this analytical solution for the hoop stress, we can see that a tensile stress should develop at the surface.

To account for the stress state in the interfacial layer, we use a finite element package, ABAQUS (2010 version), for lithiation-induced swelling with plasticity. In this model, we adopt an isotropic elastic and perfectly plastic model, using the mechanical properties shown in Table 1. Using the analogy between diffusion-induced swelling and thermal expansion, we model the phase boundary by specifying the temperature field. The total strain rate at any point is composed of the elastic ($\dot{\varepsilon}^e$), and plastic ($\dot{\varepsilon}^p$) strain rates as well as the transformation strain rate ($\dot{\varepsilon}^t$) due to lithiation. Elastic properties are assumed to be isotropic, obeying Hooke's law, and the conventional J-2 flow rule, without hardening, is used for plastic strain calculations. The amorphous Li_xSi shell expands isotropically according to the specified temperature distribution with a linear transformation strain of 0.4, which leads to about a 300% volume expansion. The reaction front thickness is taken to be much smaller than the radius. For the out-of-plane deformation, we assume a plane strain condition.
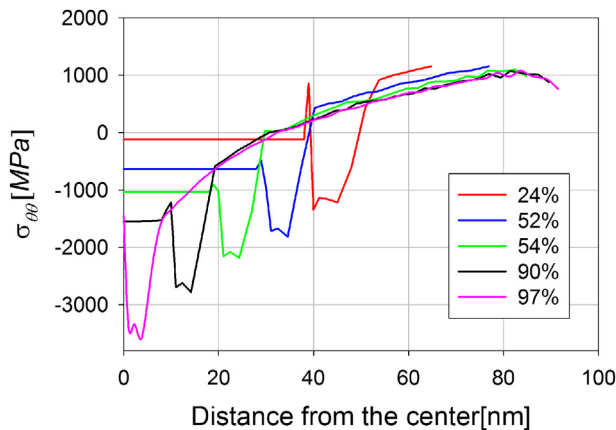
With the numerical model described above, stresses have been computed for the lithiation of a Si NP with a diameter of 100 nm. The hoop stresses are plotted in Fig. 2. It shows tensile stress developed easily at the surface due to huge volume expansion at the interfacial boundary, which provides a clear explanation for why cracking is initiated at the surface of the NPs during lithiation of crystalline Si [25], rather than from the center.

2.2. Anisotropic expansion model

Our recent experimental study revealed that lithiation of crystalline Si occurs faster in the <110> direction than other directions [18,26]. To model the anisotropic phase boundary motion, we

Table 1
Material properties and operating parameters.

Material	Description	Symbol [dimension]	Value	References
Crystalline Si	Young's modulus	E [GPa]	185	[36]
	Yield point	y [GPa]	7	[37]
	Poisson's ratio	v	0.28	[36]
Li_xSi alloy	Young's modulus	E [GPa]	35	[38]
	Yield point	y [GPa]	1	[39]
	Poisson's ratio	v	0.22	[40]

Fig. 2. Hoop stress from the isotropic expansion model of a crystalline Si pillar with initial radius of 50 nm. This plot shows the stress across the cross section from the center of the pillar to the surface at five different times during the lithiation process; legend shows the degree of lithiation.
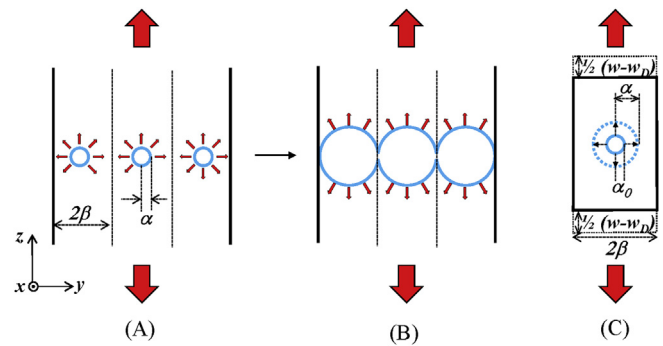
adjust the temperature field according to different crystallographic orientations of the Si core. Following experimental observations, the phase boundary on the <110> plane is assumed to move 5 times faster than that on the <100> plane and the velocities in all other directions are assumed to be much smaller.

With the prescribed temperature fields, we compute stresses and morphology changes in Si NPs with <100>,<110>, and <111> axial orientations. We observe that morphology changes according to the prescribed temperature fields are in a good agreement with experimental observations [18], as shown in Fig. 3. As expected, the stress concentration occurs midway between adjacent <110> planes, which coincides with the fracture sites in experiments. Detailed morphologies and stress evolution are presented in Supplementary movies 1, 2, and 3.
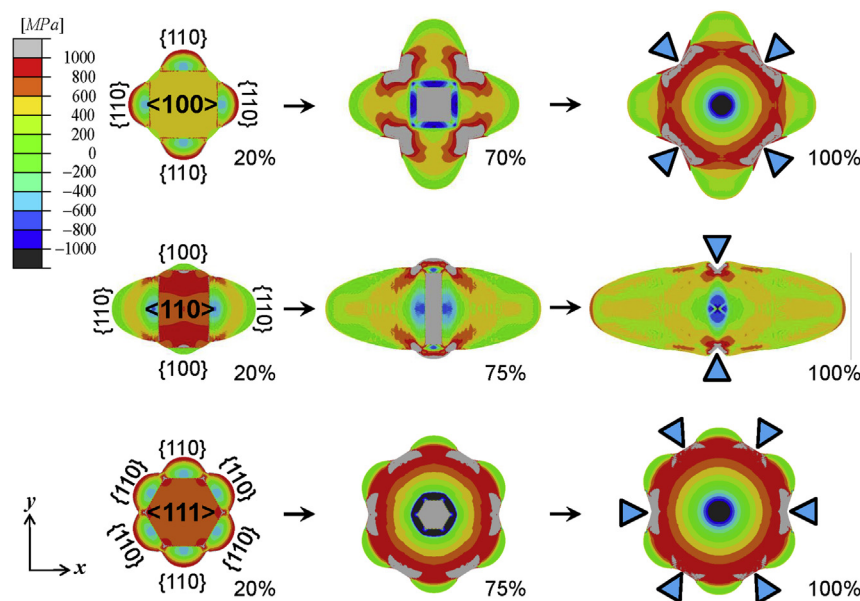
Supplementary video related to this article can be found at http://dx.doi.org/10.1016/j.jpowsour.2013.12.137.

3. Microscopic model for fracture

Based on the TEM observation that nanometer-sized pores can form during amorphization of Si [27], we developed a microscopic description of fracture based on the plastic growth of nanovoids. To explore size-dependent fracture of crystalline Si NPs upon lithiation, we use cohesive elements in the finite element method. Dugdale [28] and Barenblatt [29] first introduced the concept of cohesive zones near the crack tip and Needleman [30] developed a finite element method for the implementation of that concept. In the present model, spherical nanovoids are assumed to form in amorphous Li_xSi at a certain stress. During lithiation, the nanovoids grow and eventually link up and lead to fracture, as shown in Fig. 4A, B. For simplicity, the interaction between the voids is ignored and the spherical voids are assumed to grow in response to the hydrostatic tensile stress. As shown in Fig. 4C, we model the cohesive zone by considering hypothetical bars subjected to

Fig. 4. Schematic of the plastic void growth near the crack tip. (A) Nanovoids are formed with the radius of α and the spacing of 2β under the loading and (B) eventually linked up and lead to failure. (C) Hypothetical bar to model the hydrostatic stress state near the void. The total volume of the bar is conserved, because the volume increase at the edges is same as the volume decrease due to the void growth. α_0 is the initial radius of void and w, w_D are the separation distance at current and at the void formation, respectively.

Fig. 3. Hoop stress evolution from the anisotropic expansion model of a crystalline Si pillar with different crystallographic orientation (A) <100>, (B) <110>, and (C) <111>. The initial radius of pillars is 50 nm. Blue triangles indicate the fracture sites in the experiments. Values below figures denote the degree of lithiation and all figures are plotted with the same contour scale. (For interpretation of the references to color in this figure legend, the reader is referred to the web version of this article.)

uniaxial tensile deformation, where the void is under a hydrostatic stress state, so that it would grow isotropically, keeping the spherical shape. Afterward, when the radius of the plastic domain is same as the void spacing, the stiffness of the cohesive elements would start to be degraded.

3.1. Plastic void growth

Following the analysis of McClintock [31] for a cylindrical void, we assume that spherical voids start to form when the hydrostatic stress reaches a critical value, which is later computed from the assumed void radius α and void spacing 2β. We start by deriving the stress field of a growing spherical void in an ideally plastic solid. Due to the spherical symmetry, all variables depend only on the radial direction. The equilibrium equation and kinematic relations in the spherical coordinate system can be expressed by

$$\frac{d\sigma_{rr}}{dr} + \frac{2(\sigma_{rr} - \sigma_{\theta\theta})}{r} = 0, \ \dot{\varepsilon}_{rr} = \frac{d\dot{u}}{dr}, \ \dot{\varepsilon}_{\theta\theta} = \frac{d\dot{u}}{r}, \tag{3a,b,c}$$

where u is the displacement in the radial direction in the spherical coordinate system.

From J-2 plasticity, strain rates are expressed by

$$\dot{\varepsilon}_i = \frac{3}{2}(\sigma_i - \sigma_m)\frac{\dot{\bar{\varepsilon}}}{Y} \quad (i = rr, \theta\theta, \phi\phi) \tag{4}$$

$$\dot{\bar{\varepsilon}} = \sqrt{\frac{2}{3}\left(\dot{\varepsilon}_{rr}^2 + \dot{\varepsilon}_{\theta\theta}^2 + \dot{\varepsilon}_{\phi\phi}^2\right)}, \tag{5}$$

where σ_m is the mean stress and $\dot{\bar{\varepsilon}}$ is the effective strain rate.

Using the strain relations and equilibrium condition, the radial stress can be expressed by

$$\sigma_{rr}(\beta) = \frac{4Y}{3}\int_\alpha^\beta \frac{\dot{\varepsilon}_{\theta\theta} - \dot{\varepsilon}_{rr}}{\dot{\bar{\varepsilon}}}\frac{dr}{r}, \tag{6}$$

after using the traction boundary condition at the inner surface. From the kinematic relation and incompressibility condition, the strain rate can be expressed by

$$\dot{\varepsilon}_{rr} = -2\dot{\alpha}\frac{\alpha^2}{r^3} \tag{7a}$$

$$\dot{\varepsilon}_{\theta\theta} = \dot{\varepsilon}_{\phi\phi} = \dot{\alpha}\frac{\alpha^2}{r^3} \tag{7b}$$

$$\dot{\bar{\varepsilon}} = 2\dot{\alpha}^2\frac{\alpha^2}{r^3}, \tag{7c}$$

where $\dot{\alpha}$ is the rate of change of the void radius. Substituting these expressions into Equation (6), we get

$$\sigma_{rr}(\beta) = 2Y\log\left(\frac{\beta}{\alpha}\right) + 2\frac{\gamma_s}{\alpha}, \tag{8}$$

where γ_s is the surface energy. The last term is added to account for the effect of the surface energy of the void surface. This relation gives the hydrostatic tension stress needed to maintain plastic growth of the void; below we assume that this also corresponds to the tensile stress in the hypothetical tensile bar, as if an incompressible fluid were present above and below the growing void,

3.2. Traction–separation law

Prior to the void formation, the stress–strain relations for hypothetical bars subjected to uniaxial tensile deformation, are as described in Appendix A. To obtain the traction–separation law for this regime, we adopt these relations and estimate the total strain in z-direction as the opening displacement divided by the void spacing (β), as follows :

$$\sigma = (2\mu + \lambda)\varepsilon^{\text{total}} = (2\mu + \lambda)\frac{w}{\beta} \quad \text{(Elastic regime)} \tag{9a}$$

$$\sigma = \left(\frac{2\mu}{3} + \lambda\right)\varepsilon^{\text{total}} + \frac{2}{3}Y$$
$$= \left(\frac{2\mu}{3} + \lambda\right)\frac{w}{\beta} + \frac{2}{3}Y \quad \text{(Plastic regime)} \tag{9b}$$

where σ is the traction and w is the separation displacement of the cohesive zone and λ, μ are Lamé's constants. By equating these relations, we can find the traction (σ_P) and the separation distance (w_P) corresponding to the onset of the plasticity, as follows :

$$\sigma_P = \left(1 + \frac{\lambda}{2\mu}\right)Y, \ w_P = \frac{Y}{2\mu}\beta \quad \text{(Onset of plastic deformation)} \tag{10a,b}$$

We find the traction (σ_D) at the point of void formation by setting $\alpha = \alpha_0$, the initial void size, in Equation (8), and find the separation distance (w_D) at this point by equating the tractions in Equations (8) and (9b):

$$\sigma_D = 2Y\log\left(\frac{\beta}{\alpha_0}\right) + 2\frac{\gamma_s}{\alpha_0}, \ w_D = \frac{3\sigma_D - 2Y}{3\lambda + 2\mu}\beta \quad \text{(Void formation)} \tag{11a,b}$$

From the volume conservation during the void growth, and again imagining an incompressible fluid above and below the void, as shown Fig. 4C, we can find

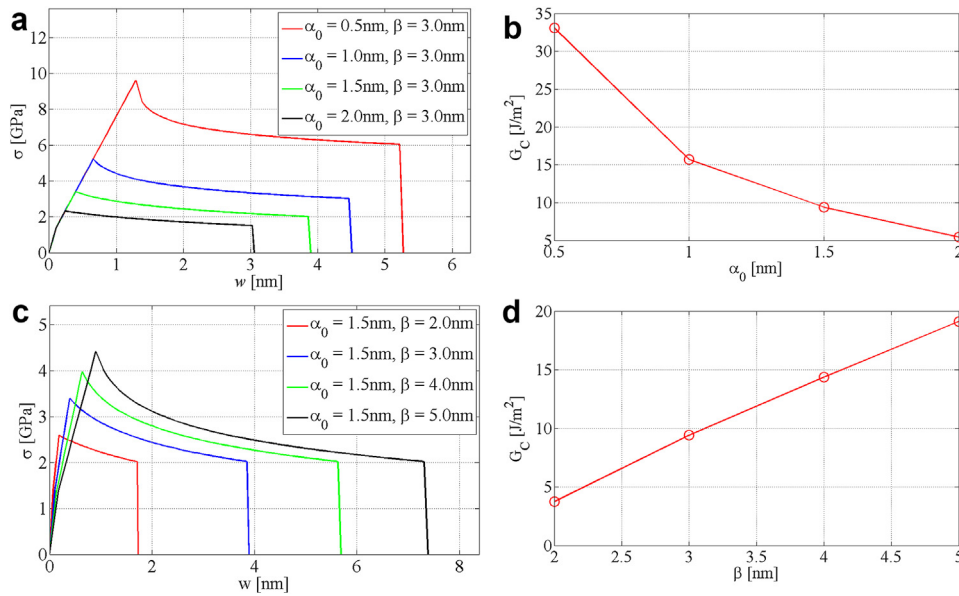$$(w - w_D)\cdot\pi\beta^2 = \frac{4}{3}\pi\left(\alpha^3 - \alpha_0^3\right). \tag{12}$$

Substituting Equation 12 into Equation (8), the traction–separation law during plastic void growth is then

$$\sigma = -\frac{2Y}{3}\log\left[\left(\frac{\alpha_0}{\beta}\right)^3 + \frac{3(w - w_D)}{4\beta}\right]$$
$$+ 2\frac{\gamma_s}{\alpha_0}\left[1 + \frac{3(w - w_D)}{4\beta}\left(\frac{\beta}{\alpha_0}\right)^3\right]^{-1/3} \quad \text{(Void growth regime)}. \tag{13}$$

As we have noted, the hydrostatic tension stress can be equated to the traction of the cohesive zone if the hypothetical bar is assumed to behave like a fluid, meaning that uniaxial loading is transmitted as the hydrostatic stress around the void. Since a cohesive element completely loses its load-carrying capacity when the void size is same as the spacing of voids, there is a maximum separation distance (w_f) which can be computed from Equation (12) by setting $\alpha = \beta$, as follows:

$$w_f = \frac{4}{3}\left(\beta - \frac{\alpha_0^3}{\beta^2}\right) + w_D \quad \text{(Maximum separation)} \tag{14}$$

Finally, the traction–separation law we will use is plotted in Fig. 5 for various values of the initial void size and their spacing. In

Fig. 5. Traction−separation law computed from the microscopic model of plastic void growth. (A) Traction−separation law and (B) accompanying fracture toughness with constant spacing of 3 nm and variable void radius. (C) Traction−separation law and (D) accompanying fracture toughness with constant initial void radius of 1.5 nm and variable void spacing.

the traction−separation law, at a given void spacing of 3 nm, G_c increases with decreasing void size (in Fig. 5A, B). In addition, G_c increases with increasing void spacing (in Fig. 5C, D) at a fixed initial void radius of 1.5 nm. These could be understood by the fact that more supporting material exists in the cohesive zone with decreasing void size and increasing void spacing.

3.3. Size-dependent fracture modeling with cohesive zone elements

With the prescribed traction−separation law, we explore the size-dependence of fracture in <100> oriented Si NPs during lithiation. Cohesive elements with zero thickness are implanted along 45°, the tilted direction between two (110) planes, where a crack is expected to propagate during lithiation due to the stress concentration in this plane. Satisfying the equilibrium conditions, cohesive elements convey traction to the adjacent elements, based on the traction−separation law, and can simulate crack initiation as well as its propagation. A detailed explanation of how to simulate crack propagation with cohesive elements is given in Appendix B.
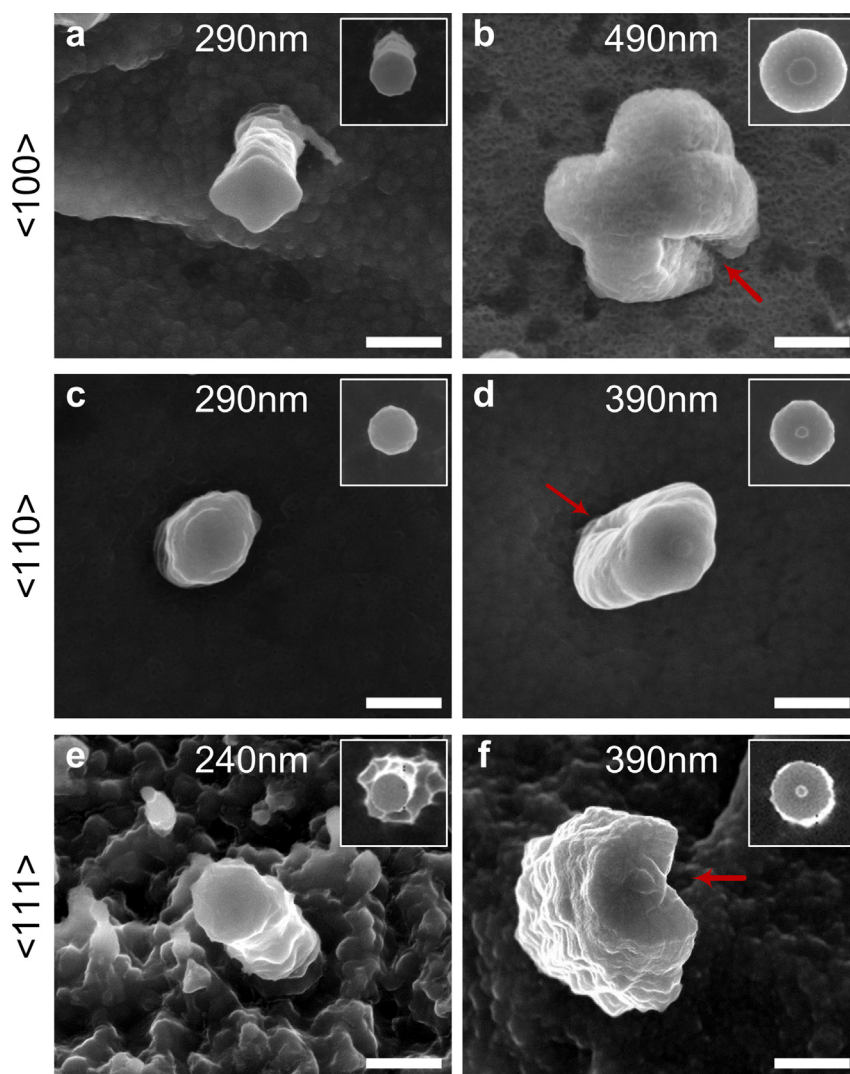
With cohesive elements, we performed simulations to estimate the G_c which would lead to the critical size of 300−400 nm, which was experimentally observed [18] in <100> oriented Si NPs during lithiation. By varying the initial void size and their spacing, we could determine whether cohesive elements completely fail at the surface according to the prescribed traction−separation law. For instance, with very low G_c, we could see the cohesive element at the surface fails and the crack propagates to the center, but for this G_c, fracture occurs easily even for small Si NPs less than 100 nm, so that the correct size dependence of fracture could not be predicted. On the other hand, with high G_c, fracture does not occur even for large Si NPs. With the void radius of 1.5 nm and spacing of 3 nm, cohesive elements on the surface completely lose their load-carrying capacity at a NP radius of 400 nm, but not at 300 nm. The approximated G_c is equal to 9.4 [J m^{-2}], which shows good agreement with recent experimental results [32].

4. Experiments

The predicted size effect on fracture of crystalline Si NPs discussed above can be compared with experiment using lithiated NPs with various crystalline axial orientations and sizes. The arrays of Si NPs were fabricated by dry etching of a single crystalline Si wafer and subsequently lithiated; fracture was observed in the scanning electron microscope (SEM) as reported previously [15]. For the lithiation, a half-cell of the pillar array and a lithium foil was made and the voltage was swept down to 10 mV (vs. Li/Li$^+$) with a sweep rate of 0.1 mV S^{-1} and then held for 10 h to reach fully lithiated state. The tested axial crystalline orientations of the Si NPs are <100> and <110> and their diameters were varied from 140 nm to 490 nm. The results for the <111> pillars are taken from our previous study [18]. Fig. 6 shows representative SEM images of lithiated Si NPs having three axial orientations with both small and large diameters to reveal the size effect on fracture. The insets show the pristine pillars with the same magnifications. All pillars consistently expand to specific shapes corresponding to their axial orientations because of the anisotropic lithiation behavior of crystalline Si, as reported in our previous study [15,18]. The relatively small pillars with diameters less than 290 nm expand without cracking, as shown in the left hand column of Fig. 6. In contrast, most of the pillars with diameters larger than 390 nm fracture and cracks propagate toward the center of the pillar, as shown in the right hand column of Fig. 6.

For a further investigation of the size effect on the fracture of Si NPs during lithiation, the fraction of cracked pillars was counted using SEM. For each of the three axial orientations and for four pillar sizes, more than 100 pillars were counted. Then, the "fracture ratio" was defined as dividing the number of fractured NPs by the total number of pillars counted. Fig. 7a shows the fracture ratio of <100> Si NPs of various diameters as a column chart. When the average diameters of the pillars are 200 and 290 nm, cracks were not found in the pillars and the overall fracture ratio was 0% after lithiation. In contrast, larger pillars, with 390 and 490 nm diameters, showed severe fracture (100% fracture ratio) after lithiation. The <110> Si pillars exhibit a similar size effect, as shown in Fig. 7b. When the average diameters of the pillars are 260 and 290 nm, cracking was not found in the pillars. But the pillars with a diameter of 360 nm showed a fracture ratio of 10% while the pillars 390 nm in diameter showed severe fracture (100% fracture ratio) after lithiation. The fracture behavior of <111> Si pillars shown in our previous report also exhibits a size effect [18]. For pillars with

Fig. 6. SEM images showing the size effect of fracture of Si nanopillars after lithiation at 10 mV for 10 h. Insets show corresponding pristine pillars with same magnification. (a) 290 nm diameter <100> pillar. (b) 390 nm diameter <100> pillar <100> pillars expand to a cross shape. (c) 290 nm diameter <110> pillars. (d) 390 nm diameter <110> pillar. <110> pillars expand to an ellipse shape. (e) 240 nm diameter <111> pillar. (f) 390 nm diameter <111> pillar. <111> pillars expand to a circular shape. All scale bars are 500 nm.
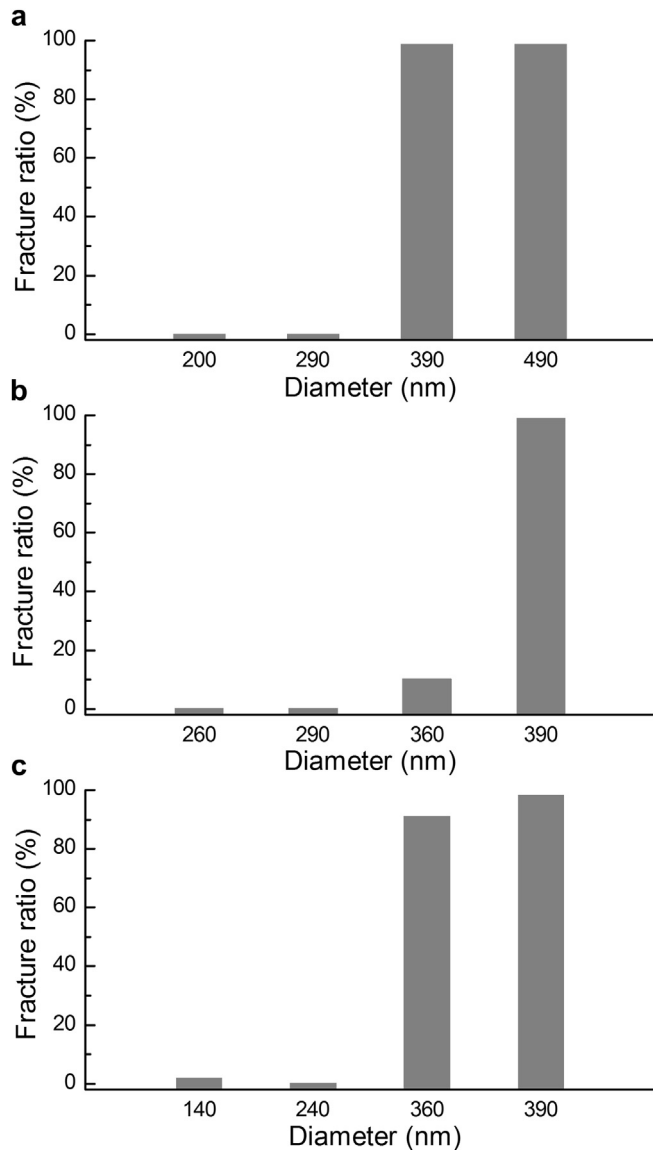
diameters of 140 and 240 nm, only a few fractures were found after lithiation and the overall fracture ratios were 2 and 0%, respectively. The larger pillars with diameters of 360 and 390 nm showed severe fracture in most of the pillars and their fracture ratios were 88 and 100%, respectively. Based on this study of the fracture ratios, it may be concluded that critical diameter for fracture of crystalline Si pillars during lithiation is between 300 and 400 nm, regardless of the axial orientation.

5. Discussion

To model the anisotropic volume expansion in Si NPs during lithiation, various approaches have been proposed. One approach involves using an anisotropic diffusivity to mimic the anisotropy of the interface reaction rate [12,19], coupled with the additional assumption of an anisotropic expansion coefficient [33]. Another approach, the one we have followed here, is based directly on the established anisotropic phase boundary motion [17]. A limitation of the former approach is that invoking an anisotropic diffusivity can lead to a misunderstanding of the physical processes involved, since the diffusivity in a cubic structure is isotropic. In addition, amorphization due to lithiation should not have any directionality

so that an anisotropic expansion coefficient is also misleading. For these reasons, we have followed the work of Pharr et al. [17] and directly modeled the anisotropic expansion with anisotropic phase boundary motion.

Due to the stress concentration that develops through the anisotropic expansion, the maximum stress would be expected to exceed the yield stress even without hardening, because of the triaxiality of the stress state; the hydrostatic stress does not affect the von Mises yield criteria. However, the maximum stress should be still limited by the yield stress both in anisotropic and isotropic cases, because a crack was observed to start to form at the surface where the surface traction should be free. Instead, the main reason for easy fragility in anisotropic expansion cases would result from the strain localization near the edge of the phase boundaries, as shown in Fig. 3 and Supplementary movies. Following the suggestion of Liang et al. [33], we conclude from this that the fragility of the lithiated Si NPs stems from the anisotropy of the lithiation reaction. Liang et al. [33] showed that lithiated Ge nanoparticles are much more fracture resistant and concluded that this fracture resistance derives from the near isotropy of the lithiation reaction. This is also consistent with our present findings.

Fig. 7. The effect of the size on the fracture ratio for nanopillars with three kinds of axial orientations, <100>, <110>, and <111>. (a) Column chart showing the fracture ratio for <100> nanopillars of different initial diameters after lithiation. Nanopillars with 390 nm and 490 nm initial diameter have a high fracture ratio (∼100%), while 200 nm and 290 nm diameter pillars have zero fracture ratio. (b) Column chart showing the fracture ratio for <110> nanopillars of different initial diameters after lithiation. Nanopillars with 390 nm initial diameter have a high fracture ratio (∼100%), while 260 nm and 290 nm diameter pillars have zero fracture ratio. 360 nm diameter pillar shows slight increment of fracture ratio (∼5%). (c) Column chart showing the fracture ratio for <111> nanopillars of different initial diameters after lithiation. Nanopillars with 360 nm and 390 nm initial diameter have a high fracture ratio (>88%), while 140 nm and 240 nm diameter pillars have low fracture ratio (<∼5%).

For the calculation of the critical size, in our previous study [34], we were able to compute the strain energy release rate, using the J-integral method [35], for pre-existing sharp cracks of all possible lengths and for all degrees of lithiation. By comparing the maximum possible strain energy release rate with the work of fracture of Si, we could determine whether a NP of that particular size would fail. However, this kind of technique cannot be used for the present problem, because it does not model the crack propagation. In addition, the critical size based on this technique is only a rough estimate because it is based on a consideration of the worst possible scenario for fracture.

Instead of using the J-integral, cohesive elements have been used to capture the size-dependence of fracture, based on the microscopic description of void growth-coalescence. However, recent *in-situ* TEM experiments show that once a crack is initiated at the surface, it appears to grow rapidly to the center [19,20], which behavior was not observed in our finite cohesive zone modeling. Instead of brittle-like fracture, as seen in the experiments, the simulations show that a crack does initiate at the surface, but it does not propagate as much as in the experiments. This discrepancy might be understood by the fact that newly-formed fractured faces could provide a new surface diffusion path for lithium atoms to reach the pristine Si, which would alter the morphology of the fracture process. Our fracture modeling does not allow for such new lithium transport pathways. In addition, McDowell et al. [20] reported that the reaction front motion could slow down due to a stress effect on the reaction kinetics at the phase boundary. Newly-formed fracture surfaces, offering a new path for lithium diffusion, would totally alter the stress state from the isotropically well constrained stress state, so that the observed slowing of the reaction front would not be observed.

In our microscopic model, we model a crack which is initiated from the surface and propagates to the center, as observed in the TEM observation. Because a crack occurred only in the fully lithiated Si, the traction–separation law would be only for fully lithiated Li–xSi. To explore the effect of lithium density in the traction–separation law, our model could be extended, by making the microscopic parameters (void size and spacing) as functions of density. However, it often requires very difficult experimental setups to get these parameters. In addition, recent experimental measurement showed that the fracture energy does not vary significantly with lithium concentration.

6. Conclusions

We make a phenomenological model for the anisotropic lithiation in crystalline Si NPs, which is governed by the kinetics of chemical reaction of lithium and pristine Si. From the model, similar topological changes could be modeled and stress concentration would occurs at the same positions where fracture was observed in experiments. In addition, using cohesive elements associated with microscopic description of void growth-coalescence, we could estimate work of fracture of Li$_x$Si alloy, which gives rise to the similar critical diameter in experiments of <100> oriented Si NPs during lithiation. These predictions are in agreement with in experiments, which reported critical size in the same range.

Appendix A. Elastoplastic deformation prior to void formation

During elastic loading, the constitutive law can be expressed by

$$\sigma_{ii} = 2\mu\varepsilon_{ii} + \lambda(\varepsilon_{xx} + \varepsilon_{yy} + \varepsilon_{zz}) \ (i = x, y, z), \tag{A.1}$$

where λ is Lamé's coefficient and μ is the shear modulus. Be subjected to uni-axial deformation, the strains in the x–y plane are zero :

$$\varepsilon_{xx} = \varepsilon_{yy} = 0. \tag{A.2}$$

With these relations, the stresses are related to the axial strain, as follows :

$$\sigma_{xx} = \sigma_{xx} = \lambda\varepsilon_{zz}, \; \sigma_{zz} = (2\mu + \lambda)\varepsilon_{zz} \quad \text{(Elastic regime)}. \tag{A.3}$$

This relation will be used to describe the first part of the traction separation law, when the hypothetical tensile bars are deforming elastically.

For the traction separation law during plastic deformation we use the *von*-Mises yield criterion. According to this criterion plastic deformation in the bar starts at

$$\sigma_{zz} = (2\mu + \lambda)\frac{Y}{2\mu} \tag{A.4a}$$

$$\varepsilon_{zz} = \frac{Y}{2\mu}, \tag{A.4b}$$

where Y is the yield stress. Now, the total strains may be divided into elastic and plastic components, as follows:

$$\varepsilon_{ii}^{\text{total}} = \varepsilon_{ii}^{\text{elastic}} + \varepsilon_{ii}^{\text{plastic}} \; (i = x, y, z). \tag{A.5}$$

Due to the symmetry in the $x-y$ plane, $\varepsilon_{xx}^{\text{elastic}} = \varepsilon_{yy}^{\text{elastic}}$, $\varepsilon_{xx}^{\text{plastic}} = \varepsilon_{yy}^{\text{plastic}}$, and the volume conservation during the plastic deformation $\varepsilon_{xx}^{\text{plastic}} + \varepsilon_{yy}^{\text{plastic}} + \varepsilon_{zz}^{\text{plastic}} = 0$, plastic strains in the $x-y$ plane can be expressed by

$$\varepsilon_{xx}^{\text{plastic}} = \varepsilon_{yy}^{\text{plastic}} = -\frac{1}{2}\varepsilon_{zz}^{\text{plastic}}. \tag{A.6}$$

With the condition that total strains in $x-y$ plane are zero, elastic strains in $x-y$ plane are then expressed by

$$\varepsilon_{xx}^{\text{elastic}} = \varepsilon_{yy}^{\text{elastic}} = \frac{1}{2}\varepsilon_{zz}^{\text{plastic}}. \tag{A.7}$$

Following Hooke's law, the stresses are expressed by

$$\sigma_{ii} = 2\mu\varepsilon_{ii}^{\text{elastic}} + \lambda\left(\varepsilon_{xx}^{\text{elastic}} + \varepsilon_{yy}^{\text{elastic}} + \varepsilon_{zz}^{\text{elastic}}\right) \quad (i = x, y, z). \tag{A.8}$$

Since the yield condition is always satisfied during plastic deformation, the von-Mises yield criterion leads to

$$\varepsilon_{zz}^{\text{plastic}} - 2\varepsilon_{zz}^{\text{elastic}} = -\frac{Y}{\mu}. \tag{A.9}$$

From this relation, the stress–strain relation in the loading direction after yielding but prior to void formation is expressed by

$$\sigma_{zz} = \left(\frac{2\mu}{3} + \lambda\right)\varepsilon_{zz}^{\text{total}} + \frac{2}{3}Y \quad \text{(Plastic regime)}. \tag{A.10}$$

Appendix B. Damage description with cohesive elements

In this work, we simulate the crack initiation and propagation using cohesive elements. Initial response of cohesive elements is assumed to be linear-elastic prior to satisfying the damage initiation criterion, which is traction approached to the specified stress (σ_D). Beyond this point, cohesive elements start to lose load-carrying capacity by degrading their element stiffness and completely fail and should be deleted from the model when the separation distance reaches to w_f. The area beneath the traction–

separation law is equal to the work of fracture (G_c) required for a crack to propagate in the context of the linear elastic fracture mechanics. It should be noted that cohesive elements only respond linear-elastically under compression, because fracture only occur under tension or shear loading.

References

[1] J.M. Tarascon, M. Armand, Nature 414 (2001) 359–367.
[2] R.F. Service, Science 332 (2011) 1494–1496.
[3] B.A. Boukamp, G.C. Lesh, R.A. Huggins, J. Electrochem Soc. 128 (1981) 725–729.
[4] L.Y. Beaulieu, K.W. Eberman, R.L. Turner, L.J. Krause, J.R. Dahn, Electrochem. Solid-State Lett. 4 (2001) A137–A140.
[5] U. Kasavajjula, C.S. Wang, A.J. Appleby, J. Power Sources 163 (2007) 1003–1039.
[6] C.K. Chan, H.L. Peng, G. Liu, K. McIlwrath, X.F. Zhang, R.A. Huggins, Y. Cui, Nat. Nanotechnol. 3 (2008) 31–35.
[7] T. Takamura, S. Ohara, M. Uehara, J. Suzuki, K. Sekine, J. Power Sources 129 (2004) 96–100.
[8] H. Haftbaradaran, X.C. Xiao, M.W. Verbrugge, H.J. Gao, J. Power Sources 206 (2012) 357–366.
[9] L.F. Cui, R. Ruffo, C.K. Chan, H.L. Peng, Y. Cui, Nano Lett. 9 (2009) 491–495.
[10] T. Song, J.L. Xia, J.H. Lee, D.H. Lee, M.S. Kwon, J.M. Choi, J. Wu, S.K. Doo, H. Chang, W. Il Park, D.S. Zang, H. Kim, Y.G. Huang, K.C. Hwang, J.A. Rogers, U. Paik, Nano Lett. 10 (2010) 1710–1716.
[11] Y. Yao, M.T. McDowell, I. Ryu, H. Wu, N.A. Liu, L.B. Hu, W.D. Nix, Y. Cui, Nano Lett. 11 (2011) 2949–2954.
[12] X.H. Liu, H. Zheng, L. Zhong, S. Huan, K. Karki, L.Q. Zhang, Y. Liu, A. Kushima, W.T. Liang, J.W. Wang, J.H. Cho, E. Epstein, S.A. Dayeh, S.T. Picraux, T. Zhu, J. Li, J.P. Sullivan, J. Cumings, C.S. Wang, S.X. Mao, Z.Z. Ye, S.L. Zhang, J.Y. Huang, Nano Lett. 11 (2011) 3312–3318.
[13] M.J. Chon, V.A. Sethuraman, A. McCormick, V. Srinivasan, P.R. Guduru, Phys. Rev. Lett. 107 (2011).
[14] J.L. Goldman, B.R. Long, A.A. Gewirth, R.G. Nuzzo, Adv. Funct. Mater. 21 (2011) 2412–2422.
[15] S.W. Lee, M.T. McDowell, J.W. Choi, Y. Cui, Nano Lett. 11 (2011) 3034–3039.
[16] K.J. Zhao, M. Pharr, Q. Wan, W.L. Wang, E. Kaxiras, J.J. Vlassak, Z.G. Suo, J. Electrochem Soc. 159 (2012) A238–A243.
[17] M. Pharr, K. Zhao, X. Wang, Z. Suo, J.J. Vlassak, Nano Lett. 12 (2012) 5039–5047.
[18] S.W. Lee, M.T. McDowell, L.A. Berla, W.D. Nix, Y. Cui, Proc. Natl. Acad. Sci. U. S. A. 109 (2012) 4080–4085.
[19] H. Yang, S. Huang, X. Huang, F.F. Fan, W.T. Liang, X.H. Liu, L.Q. Chen, J.Y. Huang, J. Li, T. Zhu, S.L. Zhang, Nano Lett. 12 (2012) 1953–1958.
[20] M.T. McDowell, I. Ryu, S.W. Lee, C. Wang, W.D. Nix, Y. Cui, Adv. Mater. 24 (2012) 6034–6041.
[21] B. Key, M. Morcrette, J.M. Tarascon, C.P. Grey, J. Am. Chem. Soc. 133 (2011) 503–512.
[22] M.S. Whittingham, Proc. IEEE 100 (2012) 1518–1534.
[23] D.B. Kao, J.P. Mcvittie, W.D. Nix, K.C. Saraswat, IEEE Trans. Electron. Dev. 34 (1987) 1008–1017.
[24] R. Hill, The Mathematical Theory of Plasticity, Oxford University Press, Oxford, 1950.
[25] X.H. Liu, L. Zhong, S. Huang, S.X. Mao, T. Zhu, J.Y. Huang, ACS Nano 6 (2012) 1522–1531.
[26] S.W. Lee, L.A. Berla, M.T. McDowell, W.D. Nix, Y. Cui, Isr. J. Chem. 52 (2012) 1118–1123.
[27] J.W. Choi, J. McDonough, S. Jeong, J.S. Yoo, C.K. Chan, Y. Cui, Nano Lett. 10 (2010) 1409–1413.
[28] D.S. Dugdale, J. Mech. Phys. Solids 8 (1960) 100–104.
[29] G.I. Barenblatt, Adv. Appl. Mech. 7 (1962) 55–129.
[30] A. Needleman, J. Appl. Mech. 54 (1987) 525–531.
[31] F.A. Mcclintock, J. Appl. Mech. 35 (1968) 363–371.
[32] M. Pharr, Z. Suo, J.J. Vlassak, Nano Lett. 13 (2013) 5570–5577.
[33] W. Liang, H. Yang, F. Fan, Y. Liu, X.H. Liu, J.Y. Huang, T. Zhu, S.L. Zhang, ACS Nano 7 (2013) 3427–3433.
[34] I. Ryu, J.W. Choi, Y. Cui, W.D. Nix, J. Mech. Phys. Solids 59 (2011) 1717–1730.
[35] J.R. Rice, J. Appl. Mech. 35 (1968) 379.
[36] J.J. Wortman, R.A. Evans, J. Appl. Phys. 36 (1965) 153.
[37] G.T.A. Kovacs, Micromachined Transducers Source Book, McGraw-Hill, Inc., New York, 1998.
[38] B. Hertzberg, J. Benson, G. Yushin, Electrochem. Commun. 13 (2011) 818–821.
[39] V.A. Sethuraman, M.J. Chon, M. Shimshak, V. Srinivasan, P.R. Guduru, J. Power Sources 195 (2010) 5062–5066.
[40] L.B. Freund, S. Suresh, Thin Film Materials, Cambridge University Press, New York, 2003.

List of symbols

a [nm]: radius of the Si core in a pressurized tube
b [nm]: outer radius of a pressurized tube
r [nm]: radial position in a pressurized tube

Y [nm]: yield stress
u [nm]: radial displacement
w [nm]: separation displacement in cohesive zone
w_P [nm]: separation displacement at onset of the plasticity
w_D [nm]: separation displacement at void formation
w_f [nm]: maximum separation displacement
G_c [J m^{-2}]: work of fracture

Greek

α [nm]: void radius
α_0 [nm]: initial void radius
$\dot{\alpha}$ [nm]: rate of change of the void radius
β [nm]: void spacing

λ [GPa]: Lamé's coefficient
μ [GPa]: shear modulus
γ_s [J m^{-2}]: surface energy
σ [GPa]: traction in cohesive zone
σ_P [GPa]: traction at onset of the plasticity
σ_D [GPa]: traction at void formation
σ_m [GPa]: mean stress
$\sigma_{xx}, \sigma_{yy}, \sigma_{zz}$ [GPa]: stresses in Cartesian coordinate system
$\sigma_{rr}, \sigma_{\theta\theta}, \sigma_{\varphi\varphi}$ [GPa]: stresses in cylindrical/spherical coordinate system
$\varepsilon^{elastic}, \varepsilon^{plastic}, \varepsilon^{total}$ [·]: strains (elastic/plastic/total)
$\dot{\varepsilon}^e, \dot{\varepsilon}^p, \dot{\varepsilon}^t$ [s^{-1}]: strain rates (elastic/plastic/transformation)
$\dot{\bar{\varepsilon}}$ [s^{-1}]: effective strain rate
$\dot{\varepsilon}_{rr}, \dot{\varepsilon}_{\theta\theta}, \dot{\varepsilon}_{\phi\phi}$ [s^{-1}]: strain rates in spherical coordinate system